Experimental study of the collision 11Be + 64Zn around the Coulomb barrier

Di Pietro, A.; Scuderi, V.; Moro, A. M.; Acosta, L.; Amorini, F.; Borge, M. J. G.; Figuera, P.; Fisichella, M.; Fraile, L. M.; Gomez-Camacho, J.; ...

Source / Izvornik: **Physical Review C - Nuclear Physics, 2012, 85**

Journal article, Published version
Rad u časopisu, Objavljena verzija rada (izdavačev PDF)

https://doi.org/10.1103/PhysRevC.85.054607

Permanent link / Trajna poveznica: https://urn.nsk.hr/urn:nbn:hr:217:246751

Experimental study of the collision ^{11}Be + ^{64}Zn around the Coulomb barrier

A. Di Pietro,[1,*] V. Scuderi,[1,2] A. M. Moro,[3] L. Acosta,[4,†] F. Amorini,[1,2] M. J. G. Borge,[5] P. Figuera,[1] M. Fisichella,[1,6] L. M. Fraile,[7] J. Gomez-Camacho,[3,8] H. Jeppesen,[9,‡] M. Lattuada,[1,2] I. Martel,[4] M. Milin,[10] A. Musumarra,[1,2] M. Papa,[1] M. G. Pellegriti,[1,2] F. Perez-Bernal,[4] R. Raabe,[11] G. Randisi,[1,2,§] F. Rizzo,[1,2] G. Scalia,[1,2] O. Tengblad,[5] D. Torresi,[1,2,12] A. Maira Vidal,[5] D. Voulot,[9] F. Wenander,[9] and M. Zadro[13]

[1]*INFN-Laboratori Nazionali del Sud and Sezione di Catania, Via S. Sofia 62, I-95123 Catania, Italy*
[2]*Dipartimento di Fisica ed Astronomia Universitá di Catania, Catania, Italy*
[3]*Departamento de FAMN, Universidad de Sevilla, Sevilla, Spain*
[4]*Departamento de Física Aplicada, Universidad de Huelva, Huelva, Spain*
[5]*Instituto de Estructura de la Materia CSIC, Madrid, Spain*
[6]*Dipartimento di Fisica ed Astronomia Universitá di Messina, Messina, Italy*
[7]*Departamento de Física Atómica, Molecular y Nuclear, Universidad Complutense, Madrid, Spain*
[8]*Centro Nacional de Aceleradores, Sevilla, Spain*
[9]*ISOLDE, CERN, CH-1211 Geneva 23, Switzerland*
[10]*Department of Physics, Faculty of Science, University of Zagreb, Zagreb, Croatia*
[11]*Instituut voor Kern-en Stralingsfysica, KU Leuven, Leuven, Belgium*
[12]*Centro Siciliano di Fisica Nucleare e Struttura della Materia, Catania, Italy*
[13]*Division of Experimental Physics Ruđer Bošković Institute, Zagreb, Croatia*

(Received 3 February 2012; published 4 May 2012)

In this paper details of the experimental procedure and data analysis of the collision of ^{11}Be+^{64}Zn around the Coulomb barrier are described and discussed in the framework of different theoretical approaches. In a previous work [A. Di Pietro *et al.*, Phys. Rev. Lett. **105**, 022701 (2010).], the elastic scattering angular distribution of the collisions ^{9,10}Be+^{64}Zn as well as the angular distribution for the quasielastic scattering and transfer/breakup cross sections for the ^{11}Be+^{64}Zn reaction were briefly reported. The suppression of the quasielastic angular distribution in the Coulomb-nuclear interference angular region observed in the collision of the ^{11}Be halo nucleus with respect to the other two beryllium isotopes was interpreted as being caused by a long-range absorption owing to the long decay length of the ^{11}Be wave function. In this paper, new continuum-discretized coupled-channel calculations of the ^{11}Be+^{64}Zn reaction are reported in the attempt to interpret the effect of coupling with the breakup channels on the measured cross sections. The calculations show that the observed suppression of the Coulomb-nuclear interference peak is caused by a combined effect of Coulomb and nuclear couplings to the breakup channels.

DOI: 10.1103/PhysRevC.85.054607 PACS number(s): 25.60.Bx, 25.60.Dz, 25.70.Bc

I. INTRODUCTION

The existence of light nuclei with a localized central core surrounded by a dilute halo of neutron or proton matter is now well established [1]. It is interesting to investigate to what extent complementary information on the structure of such nuclei and on its effect on the reaction processes can be obtained from high-quality elastic scattering angular distribution data or from the measurement of other reaction channels, such as transfer or breakup, performed at low bombarding energies. The elastic scattering of a halo nucleus from a stable target can give simple direct evidence for the structure of the halo. In the various experiments performed so far using the ^{6}He nucleus on several targets, the halo structure of such a nucleus has manifested with dramatic changes in the elastic cross section from the expected behavior (e.g., Refs. [2] and [3]) and with an overall increase in the total reaction cross section in favor of direct reaction channels.

Although elastic scattering can be described by models where the internal structure of the incoming nuclei is not explicitly taken into account [i.e., the optical model (OM)], the structure of the colliding nuclei has consequences on the outcome of the process. Indeed the elastic scattering of two nuclei is often described in terms of the Coulomb rainbow model or the Fraunhofer or Fresnel diffraction model. The first assumes no absorption; for small impact parameters the competing effects of nuclear attraction and Coulomb repulsion lead to a maximum in the deflection function and, consequently, in the cross section, usually called the Coulomb "rainbow." Diffraction models assume absorption from the elastic channel. If the Coulomb field is weak, Fraunhofer diffraction occurs as a consequence of the interference of the diffracted waves from opposite sides of the target nucleus; if the Coulomb field is strong, one has the Fresnel diffraction and only the scattering from the near side is seen. However, depending on the structure of the colliding nuclei, the angular

*dipietro@lns.infn.it
†Present address: INFN–Laboratori Nazionali del Sud, Catania, Italy.
‡Present address: Nuclear Science Division, Lawrence Berkeley National Laboratory, Berkeley, CA 94720, USA.
§Present address: Instituut voor Kern-en Stralingsfysica, KU Leuven, Leuven, Belgium.

distribution can differ completely from the above-mentioned limits [4]. For instance, if the nuclear surface of the scattering nucleus is "soft," as in the case of halo nuclei, the effect of absorption is to damp the peripheral nuclear amplitude, thus reducing the Coulomb nuclear interference peak. Moreover, the Coulomb trajectories at small impact parameters are absorbed [5].

Indeed, it is well known that, in a complete theoretical treatment of the scattering process, the internal structure of nuclei must be considered, as strong coupling to inelastic transitions, or to other reaction channels, can have important effects on the elastic scattering cross sections. This can be explicitly taken into account by performing coupled-channel calculations. Inelastic excitations, for weakly bound halo nuclei that have at most one bound excited state, correspond to coupling also to the breakup channels. This can be treated using the continuum-discretized coupled-channel (CDCC) method, an extension of the traditional coupled-channels method that, in addition to the coupling to bound states, takes into account the coupling to the unbound states of the projectile. These calculations require an accurate description of the projectile structure and the correct coupling to bound and unbound states of the halo nucleus. The CDCC method provides the elastic and breakup observables, and therefore, the availability of high-quality elastic scattering data provides a very useful test to assess the validity of the structure and reaction model assumed in the CDCC calculations and helps to set constraints on the input ingredients. Therefore, angular distributions extending over large angular ranges, with small angular steps and relatively small error bars, are needed. With radioactive beams it is not always an easy task to fulfill such requirements owing to the low intensity of such beams. In the case of the ^{6}He beam, more and more good-quality elastic scattering data on different target masses have become available. This was not the case for other halo nuclei. Recently we published a letter [6] where the quasielastic and breakup angular distributions for ^{11}Be on ^{64}Zn were reported along with the elastic scattering angular distributions of two other Be isotopes: ^{9}Be and ^{10}Be. In the present paper we describe the details of the experiment and of the theoretical analysis performed that could not be reported in Ref. [6] as well as new theoretical calculations that were performed on the same data.

II. EXPERIMENTAL DETAILS

The experiment with the ^{10}Be and ^{11}Be radioactive beams was performed at the REX-ISOLDE facility of CERN [7]. The energies of the ^{10}Be and ^{11}Be beams were 28.4 and 28.7 MeV, respectively. The ^{10,11}Be nuclei were produced in a spallation reaction of 1.4-GeV protons delivered by the CERN PSBooster, impinging on a Ta target. Beryllium atoms were extracted from the target, ionized to the 1^{+} charge state by the ISOLDE laser ion source RILIS, and mass separated in the high-resolution separator. Afterward the ions were cooled at the penning trap REX-TRAP, charge bred to the 3^{+} charge state by the electron beam ion source REX-EBIS, and postaccelerated in the REX-Linac to the required energies. The ion beam was further mass separated by a magnetic dipole placed after the REX-Linac and sent to the experimental chamber, where it collided with the reaction target. The ^{10}Be beam traversed a 550 μg/cm^2, and the ^{11}Be beam a 1000 μg/cm^2, ^{64}Zn target. The target was placed at an angle of 45° with respect to the beam direction in order to allow measurements at ≈90°. The energy of the ^{10}Be beam was chosen in order to have approximately the same center-of-mass energy of the ^{11}Be+^{64}Zn system.

The final energy resolution (energy resolution of the beam plus the energy straggling into the ^{64}Zn target) was insufficient to separate ^{11}Be elastic from inelastic scattering of the ^{11}Be first excited state at $E_x = 320$ keV, but as we see in Sec. III, the inelastic channel contributes very little to the measured angular distribution. The average beam intensity of the ^{11}Be beam was 10^4 pps and that of ^{10}Be was two orders of magnitude higher. In order to collect enough statistics with the very low intensity available, a detection system covering a large solid angle had to be used.

The presence of possible stable contaminant species in the radioactive beams delivered by REX-ISOLDE was considered before performing the experiment and actions were taken in order to minimize it during the run. In the present case, the main source of possible contaminants of the beam is the REX-EBIS ion source. Besides beryllium, a wide variety of ions may emerge from the REX-EBIS. This phenomenon is caused by residual gas contaminants inside the source that are ionized with the electron beam as well. In order to reduce the presence of such contaminants, particular care was sought in the choice of the buffer gas ions to be used in the REX-TRAP. As buffer gas an element with a q/A different from that of the ion of interest must be used. The charge state of both ^{10}Be and ^{11}Be beams was 3^{+}. In the case of ^{11}Be 3^{+}, ^{22}Ne 6^{+} is a possible contaminant, so ^{20}Ne was used as the buffer gas. On the contrary, in the case of ^{10}Be 3^{+}, one of the contaminants could be ^{20}Ne 6^{+}; during this run ^{22}Ne and ^{4}He were used as buffer gases. In the case of the ^{11}Be beam, another contaminant was ^{11}B coming from the REX-EBIS cathode. In order to strongly reduce the presence of such a contaminant, a carbon stripper foil was placed after the REX-Linac and before the last bending magnet to fully strip ^{11}Be and ^{11}B. Using the stripper foil, a ^{11}B/^{11}Be ratio of about 0.3% was measured. No other impurities were observed.

The experimental setup consisted of an array of six Si-detector telescopes, each formed by an ≈40-μm-thick, 50 × 50 mm^2, ΔE DSSSD detector (16 × 16 pixels) and an ≈1500-μm-thick single-pad E detector covering a total angular range of $10° \leqslant \theta \leqslant 150°$. Thanks to the high granularity, when allowed by the statistics, the angular distribution was obtained with a 1° step. A sketch of the setup is shown in Fig. 1. The total number of detection pixels was 1536, however, of the six detector telescopes used during the experiment, the data from only three of these (DSSSD3, DSSSD5, and DSSSD6, for a total of 768 pixels) were analyzed. For the other detectors (DSSSD1, DSSSD2, and DSSSD4), placed at more backward angles, the statistics obtained were too low. Moreover, because the target was tilted at 45°, the target holder casts a shadow in the region around 45° of detector DSSSD6, therefore some of the data from this detector could not be analyzed.

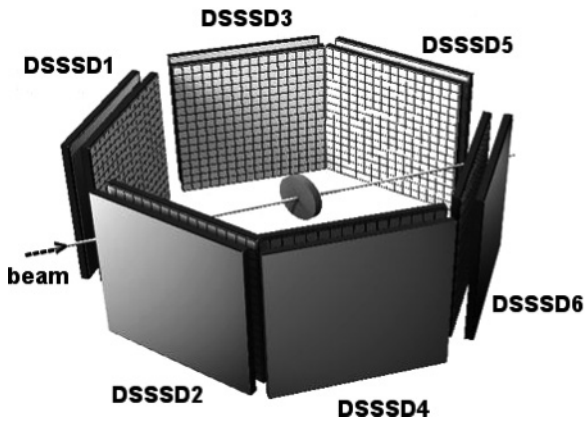

FIG. 1. Experimental setup used for the ^{10,11}Be+^{64}Zn experiment.

The two forward detectors (DSSSD5 and DSSSD6) were placed about 90 mm from the target, while the other detectors were placed at the closer distance of about 50 mm. The detection system had a very compact geometry, therefore small variations of the beam position onto the target, i.e., of the beam axis, resulted in a non-negligible variation of the detector angles. In order to properly reconstruct the angular distribution, for each run the correct geometry had to be reconstructed. To this end, we measured the elastic scattering ^{12}C,^{10}Be+^{197}Au at energies $E_{\rm cm} = 25.7$ and 27.9 MeV, respectively, for which the elastic cross section follows the Rutherford formula. The full setup was simulated; using the known geometry of the detectors, we performed a series of calculations where the angle and solid angle of each detection pixel were derived by varying the angle of the incoming beam and the impact point onto the target. For each calculation, once we determined the angle and solid angle of each pixel, we derived the ratio $\sigma_{\rm ela}/\sigma_{\rm R}$ between the elastic and the Rutherford cross section. In order to correctly take into account the beam misalignment, the input parameters of the calculations were changed to have the ratio $\sigma_{\rm ela}/\sigma_{\rm R} \approx 1$. In Fig. 2 the measured ratio between the elastic and the Rutherford cross section for the ^{12}C,^{10}Be+^{197}Au collisions is shown.

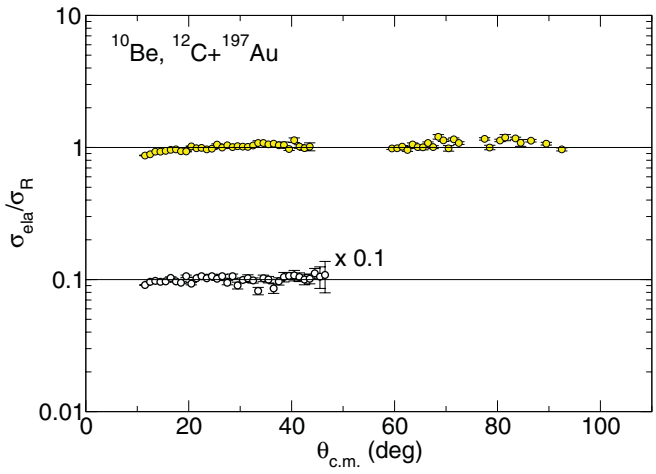

FIG. 2. (Color online) Elastic scattering angular distributions for the ^{10}Be+^{197}Au system multiplied by 0.1 (open circles) and ^{12}C+^{197}Au (filled circles). See text for details.

In the case of runs with ^{10,11}Be beams on a ^{64}Zn target, a correction was also made for the beam misalignments. This was done by looking at the small-angle elastic scattering, where the cross section is expected to be of the Rutherford type in the two front detectors (DSSSD5 and DSSSD6) placed symmetrically with respect to the beam axis.

When performing inclusive experiments at REX-ISOLDE, one has to take into consideration that the beam has a low duty cycle. Each pulse shows a macrostructure of 20 ms (50 Hz) characterized by a peak, where the beam particles are concentrated, with a width of about 50 μs. As a consequence of the time structure, the average intensity of the beam is about 400 times smaller than the instantaneous intensity. So, even though the average intensity for the ^{10}Be beam was $\approx 10^6$ pps, the instantaneous counting rate on the detectors was rather large. Because the dead time of the acquisition system was larger than the 50 μs of the burst duration, particular care had to be taken in order to control the total acquisition trigger rate, which had to be below 50 Hz. The detectors having the largest counting rate were the two placed at forward angles (DSSSD5 and DSSSD6), therefore the trigger signals coming from those detectors, in the case of the ^{10}Be beam, were opportunely downscaled in order to have a total acquisition trigger rate of $\approx$50 Hz. Another consequence of having a high instantaneous beam intensity was the possibility of having more than one elastic scattering event within the same acquisition gate. Elastic scattering events having large multiplicities (up to 4 in the ^{10}Be case and 2 in the ^{11}Be case) were acquired. The presence of these events caused some problems in the data analysis. In fact, if the energy signal of each of these elastic events was approximately the same on the ΔE detector, as was occurring in different pixels, this was not so in the residual energy detector. The residual energy detector was in fact a single-pad detector, and an energy signal equal to $\sum_{i=1}^{i=M} E_i$, where M is the multiplicity of elastic scattering in one acquisition gate and E_i the residual energy of each of the M particles, was observed. Therefore, in order to put gates on the ΔE-E plot, a different ΔE-E two-dimensional (2D) spectrum had to be produced for each multiplicity condition. We verified that if only events having multiplicity $M = 1$ were selected, the shape of the angular distribution was different than if all multiplicities were considered; this is because an $M > 1$ event is more likely to occur at forward angles, where the cross section is larger than at backward angles. Therefore, different multiplicity conditions weight in a different way at forward and backward angles. We remind the reader that multiplicity $M > 1$ events are generated by good elastic scattering events caused by beam particles being too close in time, so they must be considered in the analysis. In the data analysis, $M = 2$ events, which correspond to a signal in the interstrip region of the ΔE detector, were discarded. These events are easily identified, as they produce signals onto two adjacent strips and the amplitude of each of the two signals is lower than the energy of the elastic scattering. In the case of ^{11}Be, events corresponding to breakup or transfer were also identified. Owing to the low intensity of the ^{11}Be beam along with the small cross section of the process, only multiplicity $M = 1$ was observed for these events.

As previously mentioned, data with the stable, weakly bound ^{9}Be isotope were also gathered. The experiment with the ^{9}Be beam was performed at the Laboratori Nazionali del Sud (LNS) in Catania. A ^{9}Be beam at $E_{lab} = 29$ MeV was delivered by the 14-MV SMP Tandem of the LNS. The beam was impinging on a 550 μg/cm^2 self-supporting ^{64}Zn target that was angled at 45° to allow measurements at around 90°. In order to detect and identify ^{9}Be events produced in elastic scattering processes, five telescopes consisting of surface barrier Si detectors having a ΔE stage of $\approx$10 μm and an E stage of $\approx$200 μm were used. The experimental setup was placed in the CT2000 scattering chamber along the 60° beam line at the LNS. The five telescopes were placed on a rotating platform; thus using this system, the elastic scattering angular distribution was measured up to an angle of 110°. In order to normalize different runs having different angular settings, two monitor detectors were used as well. These were placed at fixed angles of $-20°$ and $-30°$, respectively, on the opposite side of the telescopes with respect to the beam direction. As monitors, we used 100-μm-thick surface barrier Si detectors. In order to verify the correctness of the normalization procedure, the angle covered by telescope 5 (the one placed at larger angles in the previous run) was covered by telescope 1 (the one placed at smaller angles in the following run). Using the Rutherford scattering ^{9}Be+^{197}Au (^{197}Au thickness, 145 μg/cm^2), the solid angle ratios between each telescope ($\Delta\Omega_{\mathrm{tel}_i}$) and the two monitors ($\Delta\Omega_{\mathrm{mon}_j}$) were determined. These ratios were measured at different angular settings, as the elastic cross section of ^{9}Be on ^{197}Au at $E_{\mathrm{lab}} = 29$ MeV is Rutherford at all measured angles. The final $\frac{\Delta\Omega_{\mathrm{tel}_i}}{\Delta\Omega_{\mathrm{mon}_j}}$ was the average value obtained with the different angular settings.

III. ELASTIC SCATTERING ANGULAR DISTRIBUTIONS

A comparison of the elastic scattering angular distributions of ^{9}Be+^{64}Zn and ^{10}Be+^{64}Zn is shown in Fig. 3. In Fig. 4

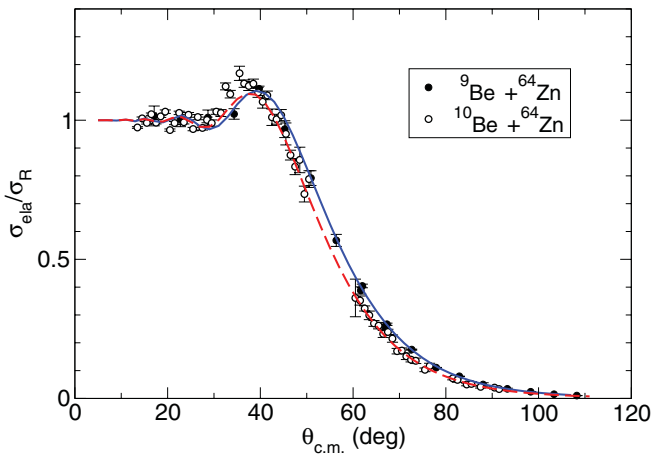

FIG. 3. (Color online) Elastic scattering angular distribution for the ^{9}Be+^{64}Zn system (filled symbols) and ^{10}Be+^{64}Zn system (open symbols). Lines represent the results of the OM analysis (see text for details).

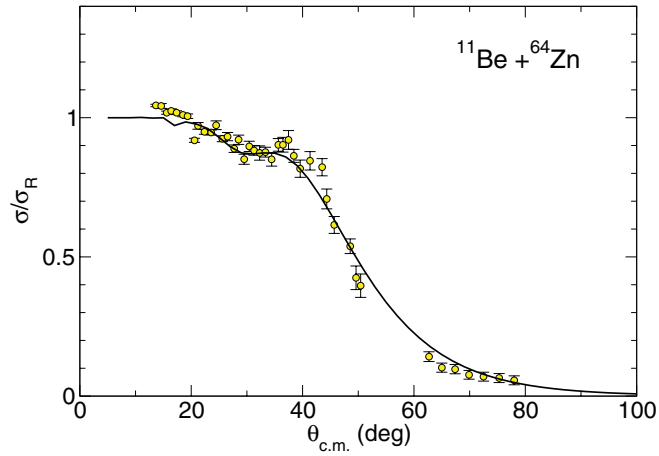

FIG. 4. (Color online) Elastic scattering angular distribution for the ^{11}Be+^{64}Zn system. The solid line represents the results of the OM analysis (see text for details).

the quasielastic angular distribution of ^{11}Be+^{64}Zn is shown. The error bars in the ^{9}Be + ^{64}Zn angular distribution include statistical plus systematic errors; the largest contribution to this error comes from the indetermination of the Rutherford cross section originating from the precision with which the angle of the monitor detectors is known (±0.05°). In the ^{10,11}Be+^{64}Zn case, only statistical errors are considered. The angular distributions were normalized to the average elastic cross sections for angles $\theta < 25°$.

As discussed in Ref. [6], the elastic scattering angular distributions of ^{9,10}Be + ^{64}Zn are very similar. Because ^{9}Be and ^{10}Be have very similar interaction radii [8], this result is not unexpected considering that, as noted in Ref. [9], the breakup channel of the weakly bound ^{9}Be nucleus at an energy of 1.4 times the Coulomb barrier does not play any role in the total reaction cross section. On the other hand, one can clearly see that, in the case of ^{11}Be+^{64}Zn, the quasielastic cross section appears to be suppressed at small angles. This feature, which cannot be attributed to the strong coupling to the bound first excited state of ^{11}Be, as this channel is included in the experimental quasielastic cross section, is typically attributed to absorption occurring at large distances. Similar shapes of the elastic scattering angular distribution have been observed before. A strong departure of the elastic cross section from the Rutherford one is observed in the case of strong long-range Coulomb $B(E2)$ excitation of either the projectile or the target, which produces absorption at large distances [4]. In the following, we try to understand the origin of such absorption in the present case.

A. Optical model analysis

A first analysis of the data was performed using the OM with the code PTOLEMY [10]. Some preliminary results of this analysis were presented in our previous letter [6]. Here, we recall the main results and provide further details. For all three systems, the projectile-target interaction was parametrized using volume Woods-Saxon (WS) shapes for both the real

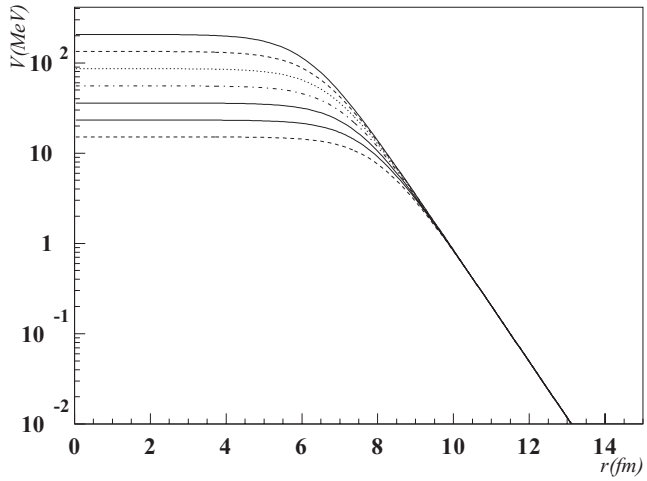

FIG. 5. Real part of the WS potentials obtained from the best-fit analysis of the ^{10}Be+^{64}Zn elastic scattering data giving equivalent χ^2 and listed in Table I.

and the imaginary parts as

$$U(r) = U_c(r, R_c) - V f_R(r, r_0, a) - iW f_W(r, r_W, a_W), \quad (1)$$

where $U_c(r, R_c)$ is the central Coulomb potential and V and W are the depths of the real and imaginary WS potentials, respectively, whose form factor is

$$f_x(r) = \{1 + \exp[(r - R_x)/a_x]\}^{-1}, \quad (2)$$

with $R_x = r_x(A_p^{1/3} + A_t^{1/3})$. The central Coulomb potential is taken as that of a uniformly charged sphere of radius $R_c = 1.25(A_p^{1/3} + A_t^{1/3})$ fm. In the case of ^{9,10}Be, the parameters of the volume potential were determined from the fit of the elastic scattering angular distribution. To avoid the inclusion of too many free parameters in the χ^2 minimization, grid searches of radius and diffuseness (real and imaginary) were made leaving the depths of the real and imaginary potentials as free parameters. The grid search was made by varying the radius and diffuseness at steps of 0.05 fm until the best χ^2 was reached. The spin-orbit potential was not included because it is well known that, for low energies, the angular distribution is weakly sensitive to the spin-orbit interaction [11].

In the case of ^{9,10}Be, when changing the geometry of the real potential, a continuous Igo-type ambiguity [12] of the optical potentials was observed. In particular, by continuously varying the radius parameter, equivalent good fits are obtained with a different potential depth. The imaginary potential remains almost unchanged. All potentials giving equivalent χ^2 are exactly the same for distances larger than about $r = 10$ fm, as shown in Fig. 5 for ^{10}Be; for all these potentials the tail is identical. This result is not surprising because, especially at the lowest energies, the elastic scattering is mostly sensitive to the tail of the nuclear potential but it does not provide information on the interior part. Therefore any set of parameters that leaves the tail of the potential unchanged will give equivalent results. In Table I, a list of the best-fit potentials that gave equivalent results, along with their χ^2 values, are shown for the ^{10}Be+^{64}Zn reaction. In Fig. 5 a comparison of the different potentials listed in Table I is shown.

TABLE I. WS OM potentials giving equivalent fits for the reaction ^{10}Be+^{64}Zn. The parameters $a = a_W = 0.7$ fm and $r_W = 1.2$ fm are the same in all potentials sets.

V (MeV)	r_0 (fm)	W (MeV)	J_V (MeV fm^3)	χ^2
207	1.00	43.07	355	8.62
133.9	1.05	43.13	263	8.62
86.31	1.10	43.22	193	8.62
55.68	1.15	43.38	141	8.63
35.96	1.20	43.61	103	8.63

In elastic scattering measurements, a typical criterion for the choice of the potentials has been the value of the volume integral of the real potential per interacting nucleon pair, defined as

$$J_V = -\frac{4\pi}{A_p A_t} \int V(r) r^2 dr. \quad (3)$$

The calculated values of J_V are listed in Table I. However, these volume integrals are energy and mass dependent, and therefore, setting constraints on them is not straightforward (see, e.g., Refs. [13] and [14]).

For the ^{11}Be+^{64}Zn system, the parametrization in terms of volume WS potentials did not provide good fits of the data. This failure was attributed to the presence of long-range couplings, as discussed previously. To account for these effects, a surface term was added to the optical potential. Physically, the volume imaginary part will be mainly connected to the scattering of the ^{10}Be core by the target and can be identified with a bare interaction describing the scattering of the ^{11}Be nucleus in the absence of excitations of the halo. These excitations are taken into account by the surface part, which can be regarded as a dynamic polarization potential (DPP) that, added to the bare potential, describes the elastic scattering of the ^{11}Be nucleus. The volume term was taken from the OM analysis of the ^{10}Be+^{64}Zn elastic scattering data. For the DPP, two types of calculations were performed. In the first one, a phenomenological surface potential was used for the DPP, parametrized in terms of the derivative of a WS potential. In the second calculation, the DPP was described using an analytic prescription that takes into account the coupling to the excited (bound or unbound) states of the projectile arising from the dipole part of the Coulomb interaction.

So, in the first calculation, the imaginary part of the DPP had the following shape:

$$V_s(r) = -4a_s \frac{df_s(r)}{dr}. \quad (4)$$

Inclusion of a real part in this DPP potential did not improve the quality of the fits and therefore it was not used. The fit of the ^{11}Be+^{64}Zn scattering angular distribution was performed having the surface potential depth as a free parameter and varying the surface diffuseness in steps of 0.05 fm. It was found that only with a diffuseness of the DPP of about $a_s \approx 3.5$ fm it was possible to reproduce the data in the

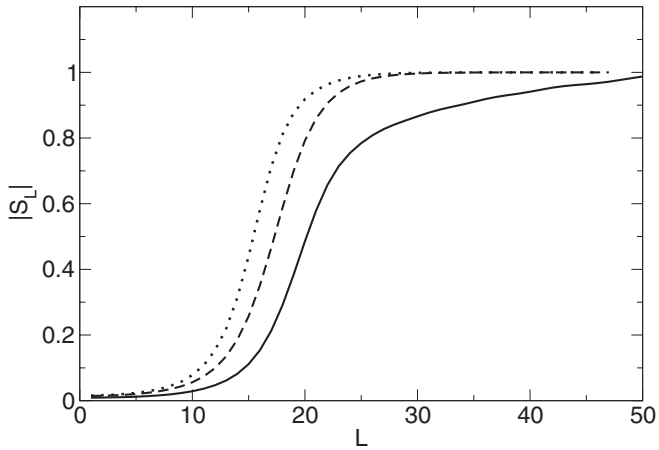

FIG. 6. Modulus of the elastic S matrix as a function of the angular momentum for ^{9}Be+^{64}Zn (dotted line), ^{10}Be+^{64}Zn (dashed line), and ^{11}Be+^{64}Zn (solid line).

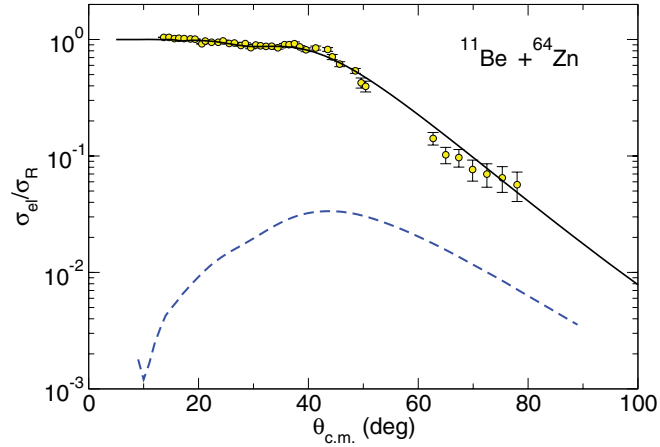

FIG. 7. (Color online) Measured quasielastic angular distribution for ^{11}Be+^{64}Zn (symbols), compared with an OM fit of the data (solid line) and a DWBA calculation (dashed line) for the inelastic scattering to the first excited state of ^{11}Be.

Coulomb-nuclear interference region and to obtain the best χ^2. Equivalent good fits, obtained by varying a_s around 3.5 fm, give the same reaction cross section within 4%. This result is in agreement with the findings of Refs. [15] and [16], where the large diffuseness was related to the decay length of the halo neutron in the ground-state wave function of ^{11}Be [15] and is responsible for the large total reaction cross section observed. A question that arises is the following: owing to the Igo ambiguity, which of the many potentials that fit the ^{10}Be+^{64}Zn elastic data should be considered for the bare potential? We verified that the ^{10}Be+^{64}Zn potentials giving the same χ^2 value also provide equivalent results for ^{11}Be+^{64}Zn, i.e., give rise to essentially the same DPP in the fit of the ^{11}Be+^{64}Zn data.

The quality of the obtained fits is shown in Figs. 3 and 4 for the set of potentials reported in Ref. [6]. Different sets of potentials giving the same χ^2 provide essentially the same angular distribution and also the same total reaction cross section. The total reaction cross sections, as quoted in Ref. [6], are $\sigma_R = 1090$ mb for ^{9}Be, $\sigma_R = 1260$ mb for ^{10}Be, and $\sigma_R = 2730$ mb for ^{11}Be. The much larger total reaction cross section obtained in the ^{11}Be case has also been reported in reactions induced by other halo nuclei such as ^{8}B and ^{6}He [3,17,18].

The moduli of the elastic scattering matrix (S-matrix) elements are shown in Fig. 6 as a function of the projectile-target orbital angular momentum. In the ^{11}Be+^{64}Zn case, the behavior of the S-matrix elements at large angular momentum values reflects the long-range absorption effect arising from the DPP extracted from the fit of the data. The OM parameters obtained from the aforementioned analysis were used for the distorted-wave Born-approximation (DWBA) calculation of the inelastic scattering angular distribution of the first excited state of ^{11}Be at $E_x = 320$ keV. The nuclear form factor used was the radial derivative of the real and imaginary OM potential obtained from the scattering data. The strength of the Coulomb transition potential was set from the experimental dipole probability $B(E1; 1/2^+ \rightarrow 1/2^-) =$ 0.115 e^2 fm^2 [19]. The calculated inelastic angular distribution is compared in Fig. 7 with the ^{11}Be+^{64}Zn quasielastic data. Although the total inelastic cross section is rather large ($\sigma_{\rm ine} \approx 400$ mb), owing to the large strength of the $B(E1)$ transition to the first excited state, it is seen that the inelastic contribution to the scattering angular distribution is very small. Therefore, the measured quasielastic scattering angular distribution corresponds mainly to the elastic scattering, with very small differences only at large angles.

The second type of OM analysis was done, as mentioned above, using as the DPP the analytic prescription proposed in Ref. [20]. This potential takes into account the effect of the coupling to the excited (bound or unbound) states of the projectile arising from the dipole part of the Coulomb interaction. The potential was derived by applying the semiclassical theory of Alder and Winther for Coulomb excitation up to the second order. The resulting DPP is complex and energy dependent, but it does not depend on the angular momentum, making its implementation in OM calculations straightforward. These calculations were done using the code FRESCO [21], with the DPP potential read externally. The only structure ingredient required by the model is the $B(E1)$ strength connecting the ground state to the dipole excited states. In the present calculations, the $B(E1)$ strength was generated with the $n-^{10}$Be potential of Capel *et al.* [22]. For the bare interaction, we kept the same volume WS used in the phenomenological OM analysis. The result of this calculation is shown by the solid line in Fig. 8. The OM calculation omitting the DPP (i.e., using only the bare potential) is also shown (dotted line). Comparing these two calculations, one sees that the dipole Coulomb couplings produce a strong reduction in the elastic cross section, approaching the calculation to the data. However, the magnitude of this reduction is not sufficient to explain the measured data. This result suggests that long-range nuclear couplings must also contribute to the further reduction in the elastic cross section at large distances. As we see in the following, this is confirmed by CDCC calculations.

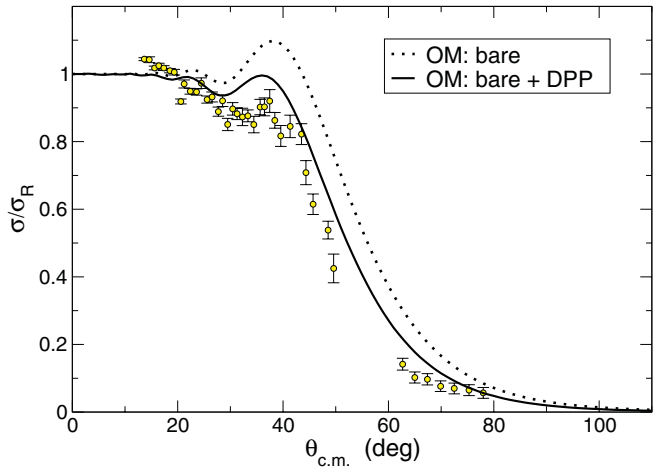

FIG. 8. (Color online) Elastic scattering angular distribution for the ^{11}Be+^{64}Zn system (symbols). The dotted line is the OM calculation performed with the bare interaction alone, and the solid line is the OM calculation adding the Coulomb DPP to the bare potential. See text for details.

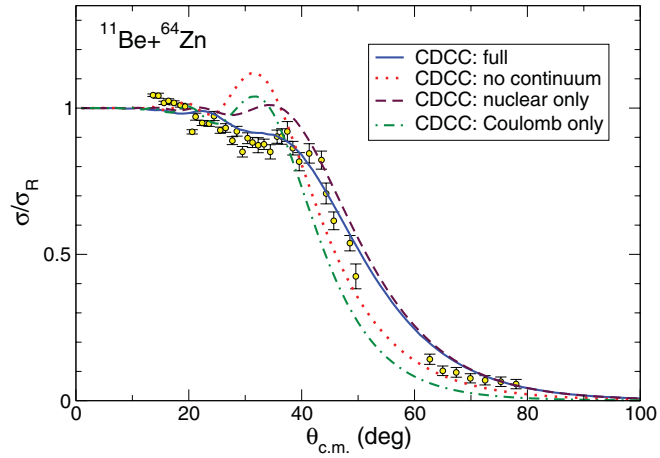

FIG. 9. (Color online) Differential quasielastic angular distributions measured in the present experiment (symbols) and CDCC calculations. The solid line is the full CDCC calculation. The dotted line is the calculation including only the ground state and first excited state of ^{11}Be. The dashed (dot-dashed) line is the CDCC calculation including only nuclear (Coulomb) breakup.

B. CDCC calculations

The measured quasielastic angular distribution has been also compared with CDCC calculations. In the CDCC method, the projectile is described in a two-body model (^{10}Be + n in this case) and coupling to breakup channels is taken into account by considering inelastic excitations of this composite projectile to the unbound states. For simplicity, we ignore the contribution of ^{10}Be excited states in the ^{11}Be states. So, within this simplified model, the ^{11}Be ground state ($1/2^+$) and the first excited state ($1/2^-$; $E_x = 320$ keV) are described, respectively, by the pure single-particle configurations $2s_{1/2}$ and $1p_{1/2}$, coupled to the ^{10}Be ground state. The continuum spectrum was discretized using the standard *binning* method. For each ^{10}Be − n partial wave (ℓ), the spectrum was truncated at a maximum excitation energy ($\varepsilon_{\max}$) and divided into a set of energy intervals (bins). For each interval, a representative normalizable wave function is constructed by averaging the continuum wave functions within the bin interval. In order to achieve full convergence of the calculated quasi-elastic cross section we needed to include n+^{10}Be partial waves up to $\ell \approx 5$, and a maximum excitation energy of $\varepsilon_{\max} = 12$ MeV, with respect to the neutron separation threshold.

The neutron-^{10}Be interaction, which is required to generate the ^{11}Be wave functions, was adopted from Ref. [22]. This potential consists of a central and a spin-orbit component, of WS shape, with a fixed geometry and a parity-dependent depth. For even partial waves, this potential reproduces the ground-state separation energy as well as the position of the $5/2^+$ resonance at $E_x = 1.8$ MeV, assuming that these states are described by pure $2s_{1/2}$ and $1d_{5/2}$ configurations, respectively. For the $\ell = 1$ states, the depth was adjusted to reproduce the separation energy of the $1/2^-$ bound excited state (assuming a $1p_{1/2}$ configuration). For other odd partial waves, we just used the depth determined for $\ell = 1$.

In CDCC, the three-body wave function (two-body projectile plus target) is expanded in the truncated model space for the internal states of the projectile. When inserted into the Schrödinger equation, this gives rise to a set of coupled differential equations, which are solved by numerical integration subject to the appropriate boundary conditions. In this set of equations, the main physical ingredients are the coupling potentials, which are generated by folding the sum of the ^{10}Be-target and neutron-target interactions with the internal states of the projectile. For the ^{10}Be-target potential, we used the optical potential extracted in Ref. [6] from the fit of the ^{10}Be+^{64}Zn elastic data. The n-^{64}Zn interaction was taken from the global parametrization of Koning and Delaroche [23], evaluated at the appropriate energy per nucleon. The coupling potentials are expanded in multipoles (λ) up to a maximum value of $\lambda_{\max} = 5$. Both nuclear and Coulomb couplings were included.

The coupled equations were solved for total angular momenta up to $J = 1000$ and up to a matching radius of 1000 fm. These calculations were performed with the code FRESCO [21].

In Fig. 9 we compare the measured quasielastic cross section with the calculations. The solid line is the full CDCC calculation. The dotted line is the calculation omitting the coupling to the continuum states, that is, including only the ground state and first excited state of ^{11}Be. Comparing these two curves, we see that the coupling to the breakup channels has a strong influence on the elastic cross section. In particular, the inclusion of these couplings produces a sizable reduction in the elastic cross section at angles of around 30°. A qualitatively similar effect has been observed in other reactions induced by weakly bound nuclei (see, e.g., Refs. [2], [18], [24], and [25],). Overall, the full CDCC calculation reproduces fairly well the data in the full angular range, although some overestimation is seen at large angles.

We have examined the contribution of the inelastic excitation of the $1/2^-$ bound state to the quasielastic cross section. This contribution is found to be relatively large

($\sigma \approx 748$ mb), about twice the value obtained from the DWBA calculations reported in the previous section. We attribute this result to the fact that the $n + {}^{10}$Be potential used in our CDCC calculations [22] gives rise to a $B(E1; 1/2^+ \rightarrow 1/2^-)$ value that is about a factor of 2 larger than the experimental value. The same overestimation is obtained with other potentials with more or less standard parameters. It has been shown that the inclusion of core-excited components in the description of the ^{11}Be nucleus yields a more realistic value of the $B(E1; 1/2^+ \rightarrow 1/2^-)$ strength. However, the inclusion of core excitation in the CDCC scheme is not straightforward [26], and no standard code is available today for this kind of calculation.

In order to disentangle the relative importance of the Coulomb and nuclear couplings to the elastic cross section, we have performed two additional CDCC calculations, one including only nuclear breakup (CDCC-nuc hereafter) and the other including only Coulomb break-up (CDCC-coul). All calculations include the monopole diagonal nuclear and Coulomb potentials derived from CDCC. The results of these calculations are depicted in Fig. 9 by the dashed and dotted-dashed lines. Compared to the no-continuum result (dotted line), it is shown that both nuclear and Coulomb couplings are responsible for the suppression of the Coulomb-nuclear interference peak, thus confirming our previous finding with the OM calculations. At larger angles, the Coulomb and nuclear breakups act in opposite directions; Coulomb couplings tend to reduce the elastic cross section, whereas nuclear couplings produce an increase in the elastic cross section with respect to the no-continuum calculation. Similar results were found in Ref. [27].

In the upper panel in Fig. 10 we present the modulus of the elastic S-matrix elements obtained from the CDCC calculations, as a function of the projectile-target orbital angular momentum, L. Note that for each total angular momentum J, two values of L are possible ($L = J \pm 1/2$), but for clarity, only the values $L = J + 1/2$ are shown. Open circles show the no-continuum calculation. CDCC calculations including either nuclear or Coulomb breakup are given by the dashed and dot-dashed lines, respectively. Finally, the solid line corresponds to the full CDCC calculation. In the lower panel in Fig. 10 the Argand plot of the elastic S matrix is depicted. It is shown that the effect of the Coulomb coupling is to reduce significantly the modulus of the elastic S matrix for large L values (e.g., $L = 25$), but it does not have an important effect on its phase. On the contrary, nuclear couplings affect the phase of the S matrix strongly. It is remarkable that, when these couplings are included, along with Coulomb couplings, the S matrix becomes approximately real. In this case, the nuclear phase shift is small, and hence the change in deflection angle is negligible. This indicates that the angular deflection owing to the attractive nuclear potential, which is responsible for the appearance of the Coulomb-nuclear interference peak, is canceled owing to the nuclear coupling to the continuum. Thus, nuclei are expected, in a semiclassical picture, to follow the Coulomb trajectory that corresponds to its impact parameter, from which they can be removed, owing mainly to Coulomb couplings.

In Fig. 11 we present the reaction, absorption, inelastic, and breakup cross sections as a function of the angular momentum

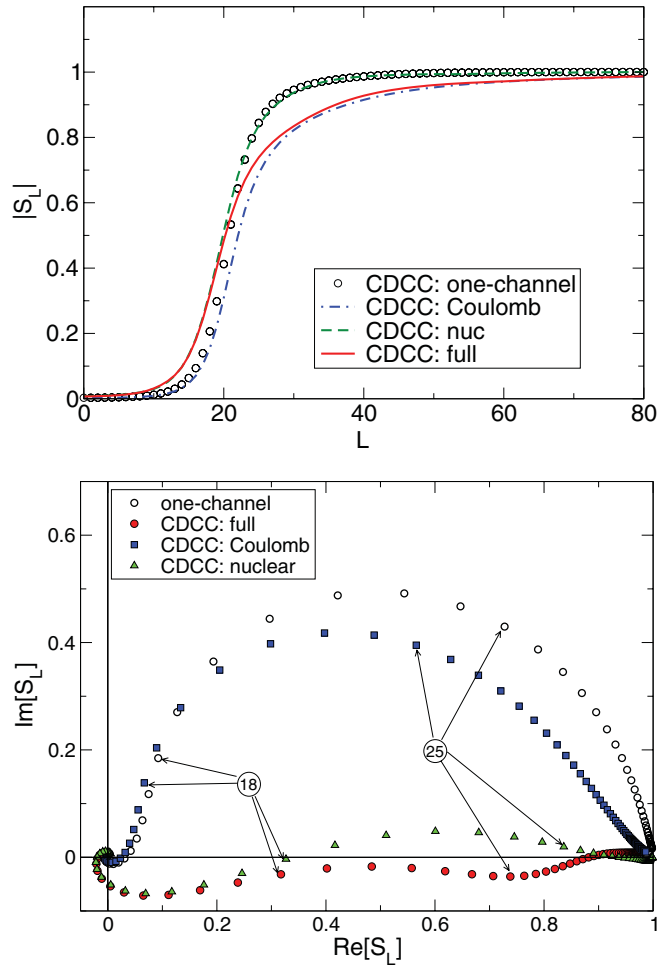

FIG. 10. (Color online) Top: Modulus of the elastic S-matrix elements as a function of the total orbital angular momentum obtained from CDCC calculations. Displayed values correspond to $L = J + 1/2$. Bottom: Imaginary versus real part of the elastic S-matrix elements for $L = J + 1/2$. The values $L = 18$ and $L = 25$ are indicated by arrows for reference.

J. Absorption cross sections are caused by the imaginary potentials included in the calculation, while inelastic and breakup cross sections are explicitly caused by the coupling. The effect of the Coulomb couplings [Fig. 11(b)] is to contribute strongly to the breakup cross section, but they do not change the absorption with respect to the one-channel (no-coupling) calculation. On the contrary, nuclear couplings [Fig. 11(a)] have a minor effect on breakup, but they do affect the absorption significantly. This effect can be understood by the fact that the nuclear couplings contribute to a smearing of the nuclear surface and cause the transit from strong absorption (for low J) to elastic scattering (for high J) to occur more gradually when nuclear couplings are included, compared to the one-channel calculation. This smearing of the nuclear surface is also responsible for the increase in the elastic scattering cross sections at large angles, which would be completely absorbed in a one-channel calculation. We see also that the inelastic cross section, which corresponds to the

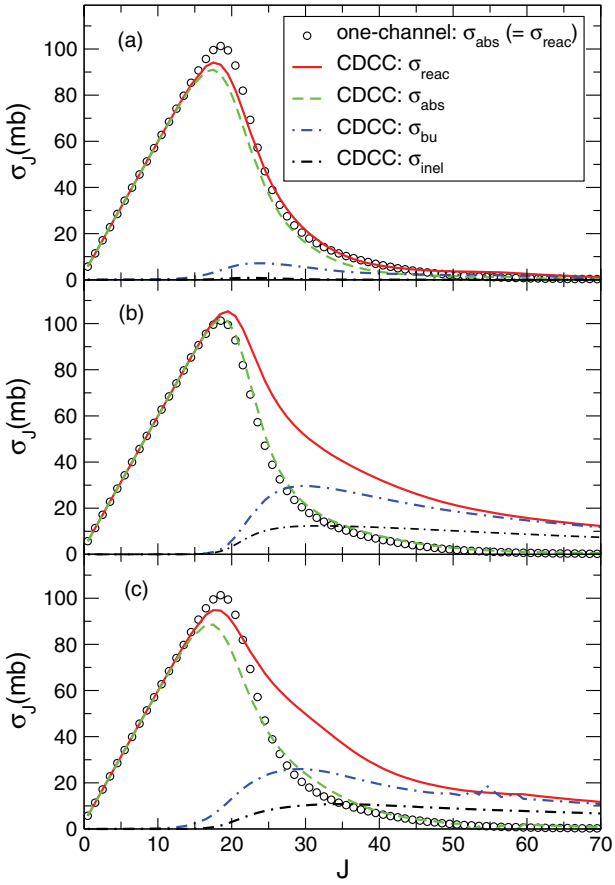

FIG. 11. (Color online) Absorption, reaction, breakup, and ^{11}Be($\frac{1}{2}^-$) inelastic cross sections obtained in CDCC calculations as a function of the total angular momentum, J. (a) The CDCC calculation including nuclear breakup, (b) the CDCC calculation with Coulomb breakup, and (c) the full CDCC calculation.

population of the $1/2^-$ excited state, is mostly caused by Coulomb couplings.

The combined effect of nuclear and Coulomb couplings, shown in Fig. 11(c), shows the smearing of the nuclear surface, which manifested in a decrease in the absorption cross sections for $J < 25$ and an increase for $J > 25$, owing to the nuclear coupling. Also observed are the breakup cross sections for large J, owing to the Coulomb coupling, which are responsible for the long-range absorption required in the OM calculation.

To finish this section, we compare our results with those presented in Ref. [28], in which a CDCC analysis of the same reaction was presented. Overall, our results are qualitatively in agreement with those in that work, but some quantitative differences are observed. Because the $n + ^{64}$Zn and ^{10}Be + ^{64}Zn interactions used in Ref. [28] are the same as those used here, the difference in the results must arise either from the structure model assumed for ^{11}Be or from the model space used in the CDCC calculations. In Ref. [28], the $n + ^{10}$Be interaction was parametrized in terms of a Gaussian shape, with the geometry adjusted to reproduce the experimental value for the $B(E1; 1/2^+ \rightarrow 1/2^-)$ probability. Moreover, those calculations were performed in a more restricted model space—$\lambda_{max} = 3$, $\ell = 0$–3, $\varepsilon_{max} = 8$ MeV—and only three bins were used for each ℓ. We have verified that these parameters are not enough for a full convergence of the quasielastic cross section. In fact, increasing the number of partial waves up to $\ell = 5$, the maximum excitation energy up to $\varepsilon_{max} = 12$ MeV, and the number of bins for each ℓ to 6, the calculated quasielastic cross section differs significantly from that presented in Ref. [28]. In particular, the quasielastic cross section is larger at the Coulomb-nuclear interference peak, overestimating the experimental data. Therefore, the damping of the Coulomb-nuclear interference peak is less pronounced with the $n + ^{10}$Be potential in Ref. [28], with respect to the analogous calculation performed with the potential adopted in the present work. A possible reason for this difference is that the ^{11}Be potential used in Ref. [28] yields a lower $B(E1)$ probability for the continuum states, compared with the one calculated with the potential in Ref. [22]. In fact, the latter is consistent with the experimental distribution measured by Palit *et al.* [29], while the $B(E1)$ calculated with the Gaussian potential underestimates the experimental distribution. So, from these tests we conclude that the approach followed in Ref. [28] to provide a reasonable value for the $B(E1; 1/2^+ \rightarrow 1/2^-)$ has the undesirable feature of also reducing the dipole couplings to the continuum. On the other hand, the approach followed here yields a $B(E1)$ distribution to the continuum in better agreement with the experimental one, but at the expense of overestimating the $B(E1)$ to the $1/2^-$ bound state. This choice seems to provide a better description of the quasielastic cross section. A more realistic approach would require taking into account the admixtures of core excited components in the description of the ^{11}Be states. This formalism was developed in Ref. [26] but so far its inherent complexity has prevented its widespread use by the community.

IV. TRANSFER AND BREAKUP

In the ^{9,10,11}Be experiments, as mentioned before, we used ΔE-E telescopes in order to distinguish scattering events from other reaction events. In this way, in the case of the ^{11}Be run, using a ΔE-E plot such as the one shown in Fig. 12, it was possible to identify, along with the scattered ^{11}Be, ^{10}Be events having an energy close to the elastic. These events correspond to transfer or breakup processes. It is important to emphasize that, as shown in Ref. [6], this type of event is not observed in the ΔE-E scatterplots for the collision induced by ^{10}Be. Unfortunately, the analysis of the above-mentioned ^{10}Be events in the ^{11}Be-induced collision could only be done for the forward detectors (DSSSD5 and DSSSD6). In the case of the detector placed at about 90°, owing to the kinematics, the energy of the Be isotopes was not sufficient to punch through the 40-μm-Si-ΔE detector, and therefore no selection between ^{10}Be and ^{11}Be could be done. Owing to the much larger contribution of the elastic and inelastic processes with respect to the transfer/breakup events, no information on the transfer/breakup cross section could be obtained by looking only at the 1D energy spectra. The angular distribution of transfer/breakup events was obtained by putting a gate on the ^{10}Be events in the ΔE-E plot. In Fig. 13 the obtained angular distribution is shown. The integrated cross section

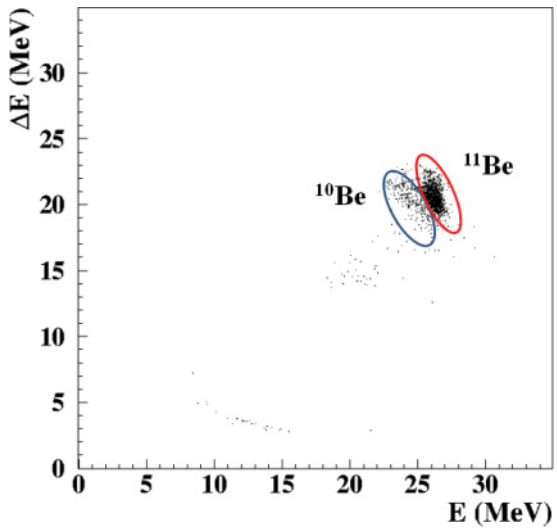

FIG. 12. (Color online) ΔE-E scatterplot for the collision ^{11}Be+^{64}Zn at $\theta = 39^{\circ}$.

obtained by assuming $d\sigma/d\Omega = 0$ at $\theta_{\rm lab} = 0^{\circ}$ and 60° is $\sigma = 1100 \pm 150$ mb. The largest contribution to the error bar comes from the extrapolation of the angular distribution $d\sigma/d\Omega$ down to 0°. An underestimation of this cross section could come from the poor resolution between ^{10}Be and ^{11}Be isotopes.

The measured angular distribution of ^{10}Be was compared with the CDCC calculations described in the previous section. For a meaningful comparison, the calculation was transformed into the laboratory frame, but approximating the scattering angle of the outgoing ^{10}Be fragment by the ^{11}Be* scattering angle. The full CDCC calculation (solid line in Fig. 13) follows a similar shape compared with the data, but the absolute magnitude is underestimated by about 30%. Part of this disagreement could be caused by the fact that the CDCC method provides only the so-called *elastic breakup*, that is, the dissociation of the projectile in which neither the core nor the valence clusters are absorbed by the target, and none of them is excited. So, for example, possible contributions coming from the transfer of the undetected valence neutron to the target or projectile breakup accompanied by target excitation are not taken into account in these calculations. Another explanation for the observed discrepancy could be the simplified single-particle model assumed for the ^{11}Be states. It is expected that a more realistic calculation, including excited components of the ^{10}Be core, would improve the description not only of the elastic data but also of the breakup data.

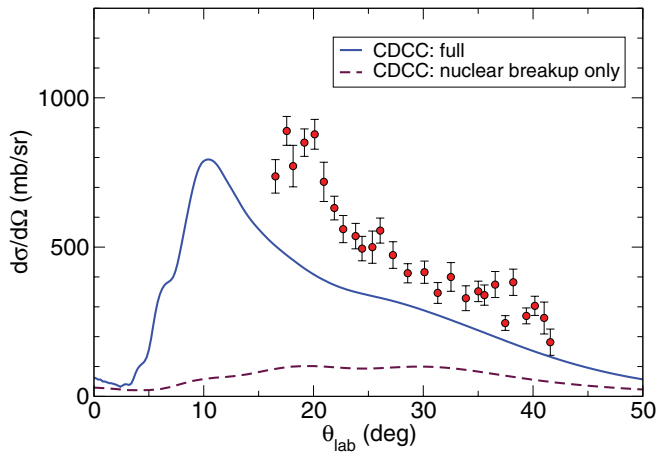

FIG. 13. (Color online) Differential cross section for the angular distribution of transfer/breakup events in ^{11}Be+^{64}Zn obtained by selecting ^{10}Be events in the ΔE-E spectrum (filled symbols). The solid line is the full CDCC calculation, whereas the dashed line is the CDCC calculation including nuclear breakup only.

We have also included the breakup distribution obtained in the CDCC calculation omitting Coulomb breakup (Fig. 13; dashed line). It is shown that the breakup cross section is reduced by a factor of almost 4, constituting further evidence of the dominance of Coulomb breakup over nuclear breakup in this reaction. We note, however, that the total breakup is not just the incoherent sum of both contributions, owing to the interference effects that appear when both kinds of couplings are included simultaneously.

V. SUMMARY AND CONCLUSIONS

In this paper details of the experimental procedure in the study of the collision ^{11}Be+^{64}Zn reported in Ref. [6] as well as new theoretical calculations are described. In Ref. [6] the elastic scattering angular distribution of the collisions ^{9,10}Be+^{64}Zn were presented, in addition to the angular distribution for the quasielastic scattering and transfer/breakup cross section for the ^{11}Be+^{64}Zn collision. The experiment with the stable ^{9}Be beam was performed at the LNS in Catania, whereas the experiments with radioactive ^{10,11}Be beams were performed at REX-ISOLDE at CERN. In the radioactive beam experiments the average beam intensity was $\approx 10^{6}$ pps for ^{10}Be and $\approx 10^{4}$ pps for ^{11}Be. Owing to the low beam intensity, a detection system covering a large solid angle was used. The detection array used was very compact, with the detectors placed very close to the target. Because of this, there was a dependence of the detection angles from the beam axis. In order to obtain the correct angular distribution, these effects were taken into consideration during the analysis. Other problems that had to be faced in the radioactive beam experiments are connected with the beam purity and the beam time structure. A beam purity better than 99% was obtained by the proper choice of buffer gas in the REX-TRAP and by introducing a carbon stripper foil just before the last bending magnet after the REX-Linac accelerator. The problem related to the time structure of the REX-ISOLDE beam was solved by keeping the total acquisition trigger rate below 50 Hz.

In these experiments the elastic scattering angular distribution for ^{9,10}Be+^{64}Zn and the quasielastic and transfer/breakup angular distributions of ^{11}Be+^{64}Zn have been measured. The data have been analyzed within the OM. In the ^{11}Be+^{64}Zn case, the data have been compared with CDCC calculations.

In the case of ^{9,10}Be+^{64}Zn OM analysis, an Igo-type ambiguity [12] of the optical potentials was found. All potentials giving the same χ^2 were the same for distances $r \geqslant 10$ fm. This is not surprising, as the elastic scattering

is a peripheral process that probes only the tail of the wave function.

In the case of the ^{11}Be+^{64}Zn data, two types of OM analyses were performed. Both analyses used as the bare potential the one obtained from the fit of the ^{10}Be+^{64}Zn data. In order to reproduce satisfactorily the measured quasielastic angular distribution, a DPP was added to the bare interaction. This DPP was derived phenomenologically in Ref. [6] using a WS derivative shape. The best χ^2 obtained required a large diffuseness of the DPP ($a_s \approx 3.5$ fm). Owing to the ambiguities found in the ^{10}Be+^{64}Zn OM analysis, it was checked that all potentials obtained from the ^{10}Be+^{64}Zn elastic scattering fit give very similar results also in the ^{11}Be+^{64}Zn case.

The second type of OM analysis performed on the ^{11}Be+^{64}Zn data used as the DPP a potential derived from the semiclassical theory of Alder and Winter for Coulomb excitation. This potential takes into account the effect of the coupling to the inelastic and breakup channels owing to the dipole Coulomb interaction. Adding this DPP to the bare interaction, a strong reduction in the elastic cross section is obtained; however, this is not sufficient to reproduce the measured data.

The measured quasielastic and inclusive breakup cross sections have also been compared with CDCC calculations, in which the ^{11}Be+^{64}Zn reaction is treated within an effective three-body model, ^{10}Be + n+^{64}Zn, and coupling to breakup channels is explicitly taken into account. These calculations clearly indicate that the suppression of the Coulomb-nuclear interference peak observed in the quasielastic distribution around 30° is caused by a combined effect of Coulomb and nuclear coupling to breakup channels, although they act in very different ways. Coulomb couplings make a large contribution to the breakup cross section, thus increasing the reaction cross section and reducing the elastic cross section accordingly. On the other hand, the nuclear breakup cross section is found to be relatively small, but these couplings have a sizable effect on the elastic phase shift, thus also affecting the elastic angular distribution. Overall, the calculation reproduces well the shape of the quasielastic angular distribution, but some overestimation is observed at angles beyond $\theta_{cm} = 40°$. Moreover, the shape of the angular distribution of outgoing ^{10}Be fragments is reasonably well reproduced by the CDCC calculations, although the magnitude is underestimated by ≈30%. We attribute this disagreement to the neglect of nonelastic breakup processes or to the simplified structure model used for the ^{11}Be nucleus. We have also shown that, when Coulomb breakup is switched off, the breakup cross section is reduced by a factor of 4, indicating that the main contribution to the calculated breakup cross section comes from Coulomb breakup.

ACKNOWLEDGMENTS

The authors wish to thank Dr. A. Bonaccorso, Professor A. Vitturi, and Professor G. Pollarolo for useful discussions. This work was partially supported by the INFN and by the Spanish Ministerio de Ciencia e Innovación under Project Nos. FPA2009-07653, FPA2009-07387, and FPA2010-17142 and by the European Commission via FP6 EURONS (Contract No. 506065).

[1] A. Jensen *et al.*, Rev. Mod. Phys. **76**, 215 (2004).
[2] A. M. Sánchez-Benítez *et al.*, Nucl. Phys. A **803**, 30 (2008).
[3] A. Di Pietro *et al.*, Phys. Rev. C **69**, 044613 (2004).
[4] W. Love *et al.*, Nucl. Phys. A **291**, 183 (1977).
[5] S. Fricke *et al.*, Nucl. Phys. A **500**, 399 (1989).
[6] A. Di Pietro *et al.*, Phys. Rev. Lett. **105**, 022701 (2010).
[7] D. Voulot *et al.*, Nucl. Instrum. Methods B **266**, 4103 (2008).
[8] I. Tanihata, H. Hamagaki, O. Hashimoto, Y. Shida, N. Yoshikawa, K. Sugimoto, O. Yamakawa, T. Kobayashi, and N. Takahashi, Phys. Rev. Lett. **55**, 2676 (1985).
[9] P. Gomes *et al.*, Phys. Rev. C **71**, 034608 (2005).
[10] M. Rhoades-Brown, M. H. Macfarlane, and S. C. Pieper, Phys. Rev. C **21**, 2417 (1980).
[11] F. Becchetti and G. Greenless, Phys. Rev. **182**, 1190 (1969).
[12] G. Igo, Phys. Rev. Lett. **1**, 72 (1958).
[13] M. Matoba, M. Hyakutake, and I. Kumabe, Phys. Rev. C **32**, 1773 (1985).
[14] A. Nadasen *et al.*, Phys. Rev. C **39**, 536 (1989).
[15] A. Bonaccorso and F. Carstoiu, Nucl. Phys. A **706**, 322 (2002).
[16] M. Y. M. Hassan, M. Y. H. Farag, E. H. Esmael, and H. M. Maridi, Phys. Rev. C **79**, 064608 (2009).
[17] E. Aguilera *et al.*, Phys. Rev. C **79**, 021601(R) (2009).
[18] E. F. Aguilera *et al.*, Phys. Rev. C **63**, 061603 (2001).
[19] F. Ajzenberg-Selove, Nucl. Phys. A **506**, 1 (1998).
[20] M. V. Andres, J. Gomez-Camacho, and M. A. Nagarajan, Nucl. Phys. A **579**, 273 (1994).
[21] I. J. Thompson, Comput. Phys. Rep. **7**, 167 (1988).
[22] P. Capel, G. Goldstein, and D. Baye, Phys. Rev. C **70**, 064605 (2004).
[23] A. J. Koning and J. P. Delaroche, Nucl. Phys. A **713**, 231 (2003).
[24] O. R. Kakuee *et al.*, Nucl. Phys. A **765**, 294 (2006).
[25] E. F. Aguilera *et al*, Phys. Rev. Lett. **84**, 5058 (2000).
[26] N. C. Summers, F. M. Nunes, and I. J. Thompson, Phys. Rev. C **74**, 014606 (2006).
[27] L. Acosta *et al.*, Phys. Rev. C **84**, 044604 (2011).
[28] N. Keeley, N. Alamanos, K. W. Kemper, and K. Rusek, Phys. Rev. C **82**, 034606 (2010).
[29] R. Palit *et al.*, Phys. Rev. C **68**, 034318 (2003).